Supporting Information for

Systematic Coarse-Grained Lipid Force Fields with Semiexplicit Solvation via Virtual Sites

Alexander J. Pak, Thomas Dannenhoffer-Lafage, Jesper J. Madsen, and Gregory A. Voth*

Department of Chemistry, The University of Chicago, Chicago, IL, USA

A Detailed Description of the REM Optimization Procedure

First, we describe the potentials we used to initialize optimization of the 7-site REM models. Recall that we use the optimized potentials for the 6-site REM model as the initial guess for the non-SL interactions. However, we must provide an initial guess for the SL-associated interactions. To do so, we use Boltzmann inversion (= $-k_BT \ln(P[r_{ij}])$), or BI; the SL-HG bond and SL-HG-MG angle potentials were also fit using BI. We note that we also tested the use of a soft excluded volume potential (= $[1+\cos(\pi r_{ij}/r_c)]$, $r_{ij} < r_c$ Å) as an initial guess for the nonbonded interactions. This functional form was chosen based on its similarity to the BI solutions found for the SL-T1 and SL-T2 interactions, which are inherently long range. This latter strategy is also acceptable, but we did find the former strategy to be more efficient, i.e., require fewer iterations. Finally, we found that the potentials for SL-T1 and SL-T2 tended to fluctuate between many solutions during optimization, which may be due to the fact that these pairwise statistics are rarely sampled. Interestingly, removing these interactions from optimization significantly improved convergence, thereby suggesting that their inclusion in the model may have introduced a degree of overfitting. Indeed, using either of the trial potentials for SL-T1 and SL-T2 had negligible effect on the predicted CG interactions and behavior of the resultant CG models (see e.g., the RDFs in Figure S3 below).

Several issues were encountered during optimization, which led to the application of the following heuristics. During optimization, intermediate solutions for the effective CG interactions are not guaranteed to yield a stable simulation. In part, this is due to the expressiveness of B-splines. Other functional forms, such as Lennard-Jones interactions, tend to conserve certain features, e.g., a rapid decay to zero at large distances and a sharp, repulsive wall followed by a global minimum at pair distances close to σ. However, B-splines are inherently local with each pair of control points (and

associated basis functions) having a considerable influence on each locally-fit potential. Hence, if a large change to a spline coefficient is prescribed during optimization, such as in regions with sharply varying pairwise density or near zero density (both of which are evident near the excluded-volume portion of a potential), large pairwise forces may also result, which contribute to numerical instability. To mitigate this issue, we downscale the change applied to any spline coefficient within a given pairwise potential to a maximum of ±0.1 kcal/mol. In this event, we rescale associated spline coefficients by the same ratio. We apply an additional smoothing to temper unreasonably large fluctuations by averaging each spline coefficient with its neighbors ($c_i = (c_{i-1} + c_i + c_{i+1})/3.0$). Finally, we affix the final spline coefficient to its initial value to ensure that each pairwise force decays to zero at its cutoff.

Table S1. Summary of CG mapping and effective masses used in this work.

	DOPC		DPPC	
Label	**Atom Indices**	**Mass (g/mol)**	**Atom Indices**	**Mass (g/mol)**
HG	1 – 24	182	1 – 24	182
MG	25 – 44	157	25 – 44	157
T1	45 – 66	110	45 – 65	98
T2	67 – 91	113	66 – 87	99
T1	92 – 113	110	88 – 108	98
T2	114 – 138	113	109 – 130	99

Table S2. Summary of the number of REM iterations used for each model.

Procedure	**DOPC-6**	**DOPC-7V**	**DPPC-6**	**DPPC-7V**
Step 1: Stochastic Subset	100	50	100	50
Step 2: All Interactions	100	100	100	100
Step 3: Stochastic Subset	50	50	50	50
Step 4: All Interactions	50	48	19	56

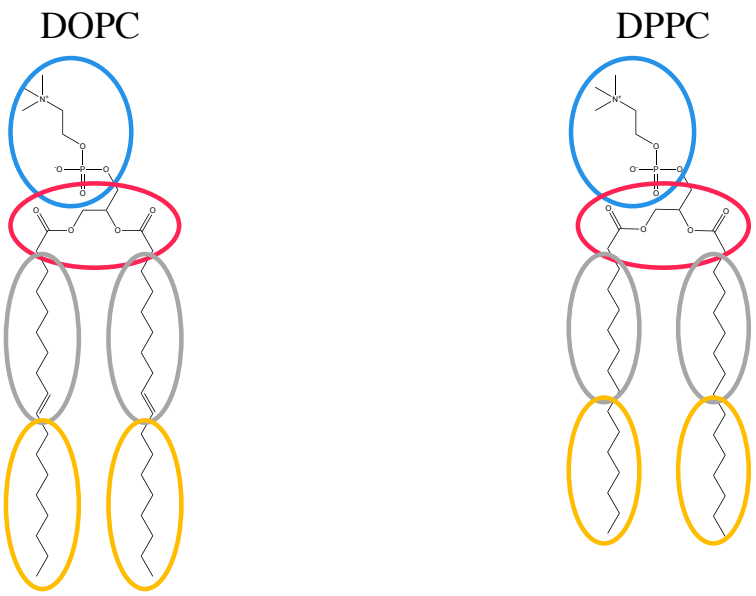

Figure S1. Schematic representation of the mapping used to represent each 6-site CG lipid model used in this work. See Table S1 for additional details.

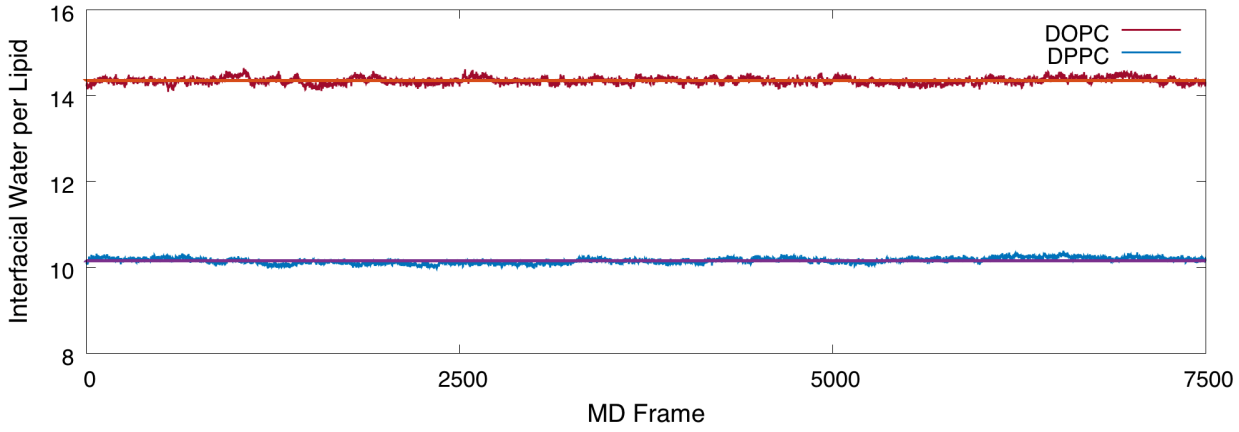

Figure S2. Time-series of interfacial (or tightly-bound) water near each head group for DOPC and DPPC. The solid line indicates the average number of interfacial water per lipid (14.4 and 10.2 for DOPC and DPPC, respectively), which was used to assign effective CG masses to the virtual SL site (260 and 183 g/mol for DOPC and DPPC, respectively).

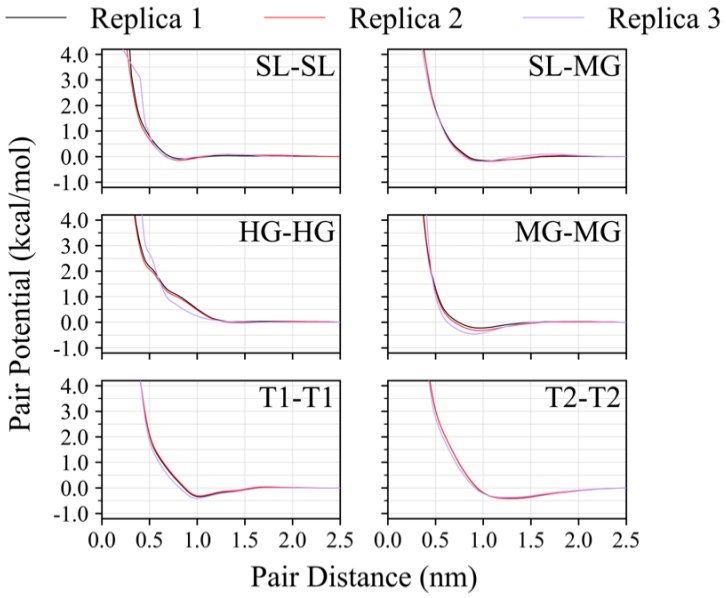

Figure S3. Comparison between REM-7V solutions for DOPC using MSCG-6 potentials (replicas 1 and 2) and generic Cooke-Deserno potentials tabulated as splines (σ = 9 Å, ε = 0.83 k_BT, w_c = 1.4σ; replica 3) as initial conditions. Only the listed pairwise nonbonded interactions are shown for clarity.

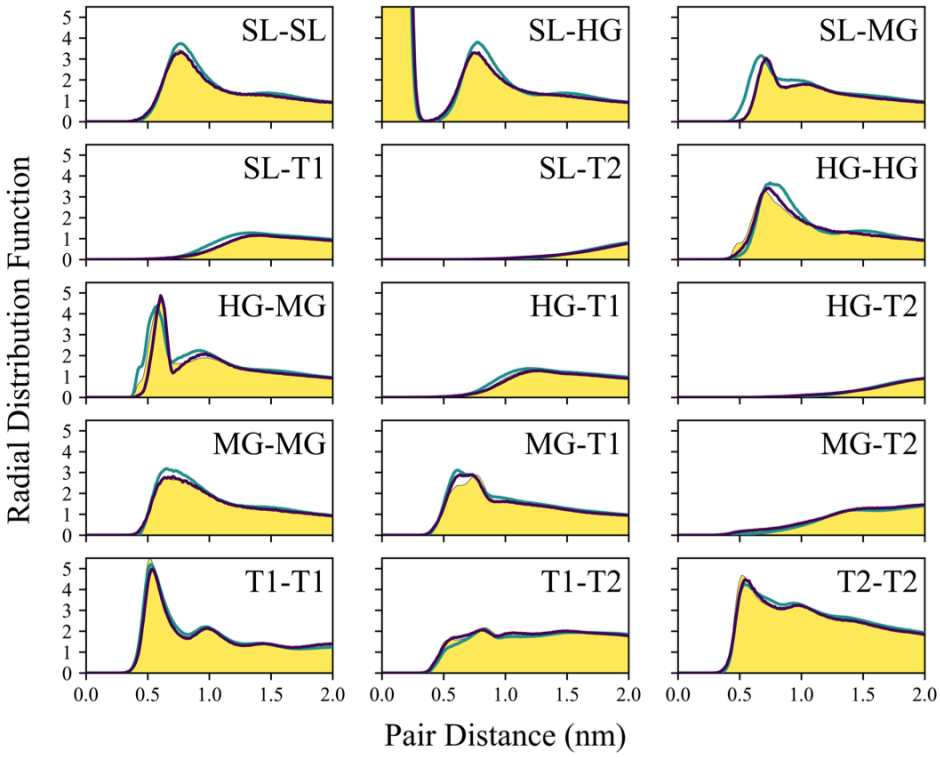

Figure S4. Comparison of the radial distribution functions calculated from the MSCG-7V (green line), REM-7V (purple line), and mapped atomistic (shaded yellow region) trajectories for DOPC.

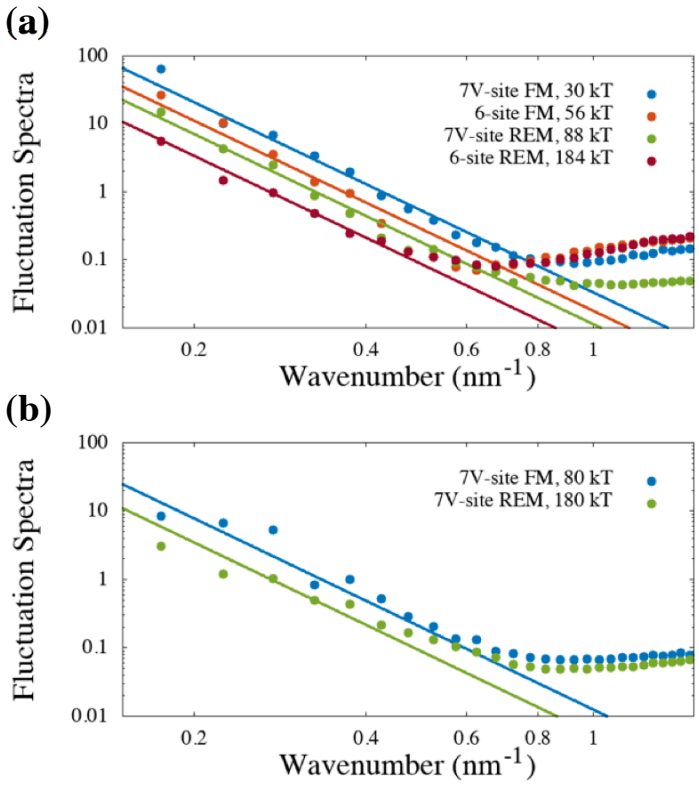

Figure S5. Height fluctuation spectra as a function of wavenumber for (a) DOPC and (b) DPPC using the listed CG model type. The solid lines indicate the fit to the low-frequency modes to obtain bending stiffness (as listed in thermal units, *kT*).

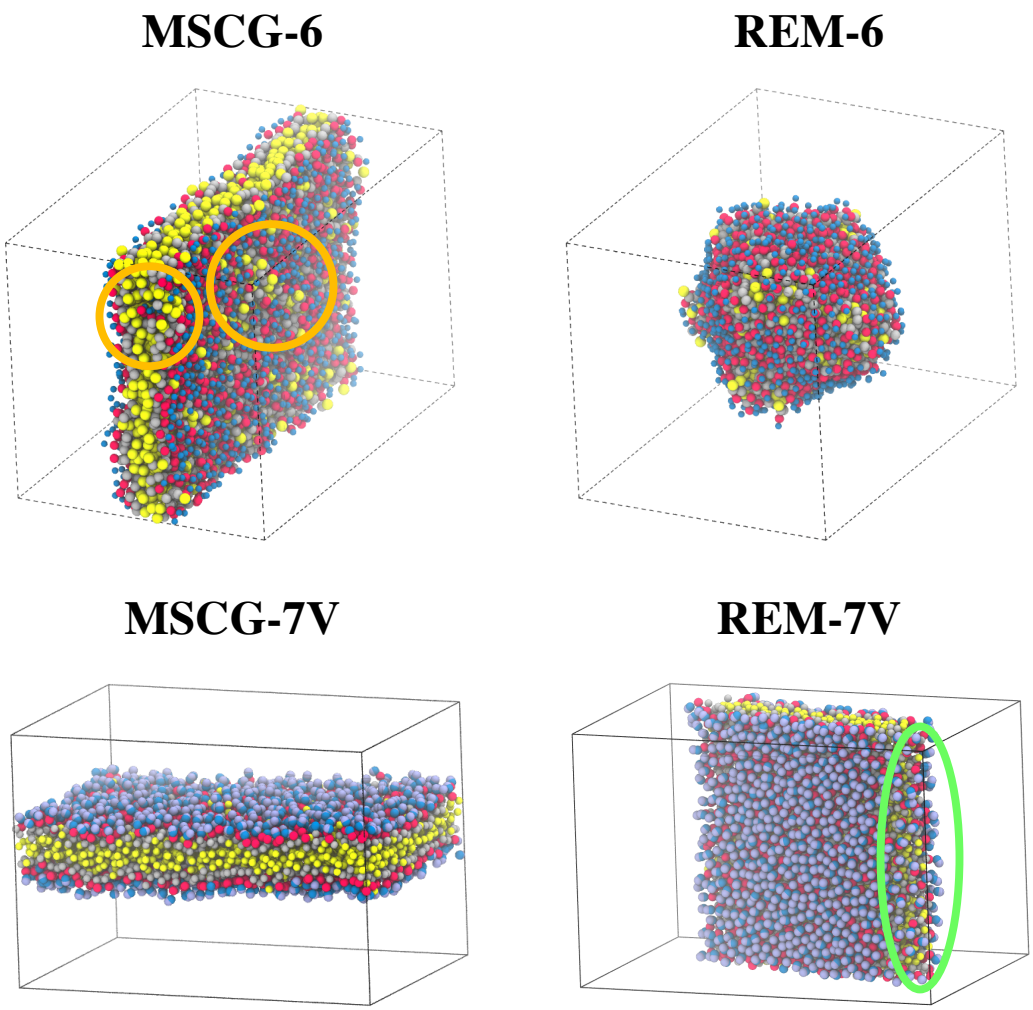

Figure S6. Endpoint snapshots after simulated self-assembly of each listed CG model for DOPC. In the MSCG-6, the orange circles highlight small defects that emerge, which include lipid headgroups embedded in the hydrophobic tail region and surface defects with protruding tails. In the REM-7V panel, the green circle highlights the "edge" of a self-assembled bilayer patch, as seen by the lipid head groups wrapping around the bilayer patch. Colors are consistent with the main text.

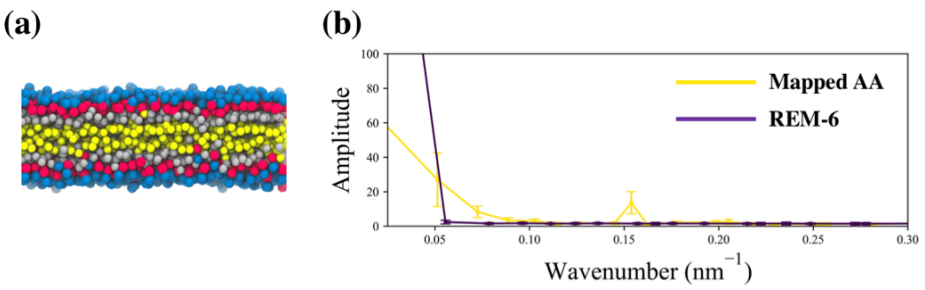

Figure S7. (a) Endpoint snapshot (from the side) of an equilibrated DPPC bilayer using the REM-6 CG model. The absence of lateral heterogeneity in height (i.e., ripples) is notable. In contrast, the DPPC-7V models appear to recapitulate rippling behavior, as discussed in the main text. Colors are consistent with the main text. (b) Comparison of amplitudes from the fast Fourier transform of the bilayer surface morphologies (taken with reference to the MG bead [red] height) generated by each model. The absence of Fourier modes generated by the REM-6 model confirms the absence of ripples.

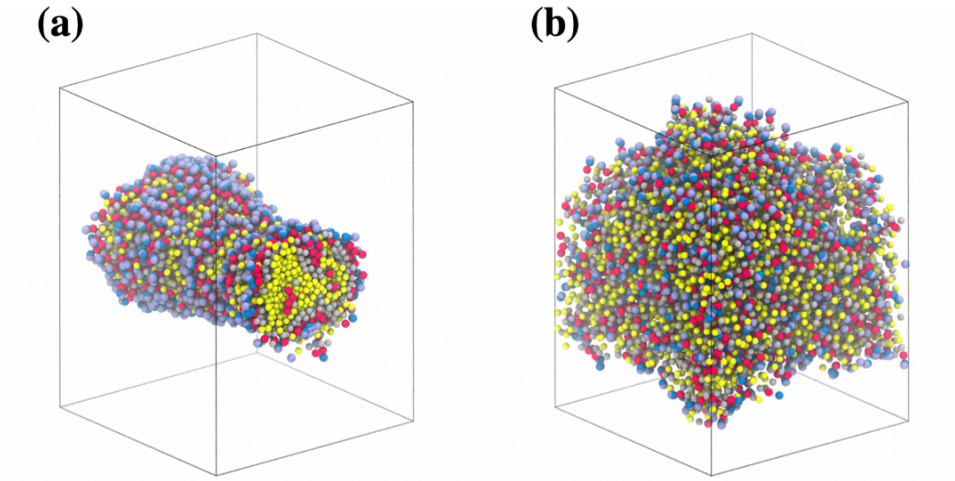

Figure S8. Snapshots of bilayer instability observed for the DPPC CG (a) REM-7V and (b) MSCG-7V models when SL beads are switched to a non-interacting state. Colors are consistent with the main text.

Movie S1. Self-assembly of DOPC-7V (MSCG-7V) lipids from an initially dispersed state into a vesicle over 1.5×10^7 MD timesteps. A clipping plane through the center of the simulation domain is used to aid visualization of the interior of the vesicle and the hydrophobic region of the vesicle bilayer (yellow beads). Throughout the movie, it is evident that lipids coalesce into spherical aggregates that eventually merge and reconstruct into the final vesicle. Colors are consistent with the main text.